scientific reports

Check for updates

OPEN

# Ab initio prediction of semiconductivity in a novel two-dimensional $Sb_2X_3$ (X= S, Se, Te) monolayers with orthorhombic structure

A. Bafekry[1,2]✉, B. Mortazavi[3], M. Faraji[4], M. Shahrokhi[5], A. Shafique[6], H. R. Jappor[7], C. Nguyen[8], M. Ghergherehchi[9]✉ & S. A. H. Feghhi[1]

**$Sb_2S_3$ and $Sb_2Se_3$ are well-known layered bulk structures with weak van der Waals interactions. In this work we explore the atomic lattice, dynamical stability, electronic and optical properties of $Sb_2S_3$, $Sb_2Se_3$ and $Sb_2Te_3$ monolayers using the density functional theory simulations. Molecular dynamics and phonon dispersion results show the desirable thermal and dynamical stability of studied nanosheets. On the basis of HSE06 and PBE/GGA functionals, we show that all the considered novel monolayers are semiconductors. Using the HSE06 functional the electronic bandgap of $Sb_2S_3$, $Sb_2Se_3$ and $Sb_2Te_3$ monolayers are predicted to be 2.15, 1.35 and 1.37 eV, respectively. Optical simulations show that the first absorption coefficient peak for $Sb_2S_3$, $Sb_2Se_3$ and $Sb_2Te_3$ monolayers along in-plane polarization is suitable for the absorption of the visible and *IR* range of light. Interestingly, optically anisotropic character along planar directions can be desirable for polarization-sensitive photodetectors. Furthermore, we systematically investigate the electrical transport properties with combined first-principles and Boltzmann transport theory calculations. At optimal doping concentration, we found the considerable larger power factor values of 2.69, 4.91, and 5.45 for hole-doped $Sb_2S_3$, $Sb_2Se_3$, and $Sb_2Te_3$, respectively. This study highlights the bright prospect for the application of $Sb_2S_3$, $Sb_2Se_3$ and $Sb_2Te_3$ nanosheets in novel electronic, optical and energy conversion systems.**

The chalcogenide compounds have attracted great interest owing to their high thermoelectric performance, microelectronics, electronic and optical properties[1–5]. For implementations in all industrial sectors, chalcogenides are presently quite interesting[6]. In this regard, the main technique in the manufacture of two-dimensional (2D) materials is the peeling of layered bulk crystals to produce few-layer flakes or monolayer (single-layer), and it has become the best method in the fabrication of high-quality sheet for several applications[7,8]. There is a large number of monolayers that used in nanodevices, catalysis, field-effect transistors, batteries, hydrogen evolution, and supercapacitors are based on the exfoliated layered materials, for example but not limited to, $Bi_2Se_3$ and $Bi_2Te_3$[9], $MoS_2$[10], $WS_2$ and $MoSe_2$[11], $MoTe_2$[12], $WSe_2$[13], CaGe[14], $MnPS_3$ and $MnPSe_3$[15,16]. The importance of these thin-layer or single-layers is that they can be considered as the starting materials for further manipulation of

[1]Department of Radiation Application, Shahid Beheshti University, Tehran, Iran. [2]Department of Physics, University of Antwerp, Groenenborgerlaan 171, 2020 Antwerp, Belgium. [3]Chair of Computational Science and Simulation Technology, Institute of Photonics, Department of Mathematics and Physics, Leibniz University of Hannover, Appelstrae 11, 30157 Hannover, Germany. [4]Micro and Nanotechnology Graduate Program, TOBB University of Economics and Technology, Sogutozu Caddesi No 43 Sogutozu, 06560 Ankara, Turkey. [5]Department of Physics, Faculty of Science, University of Kurdistan, Sanandaj 66177-15175, Iran. [6]Department of Physics, Lahore University of Management Sciences, Lahore, Pakistan. [7]Department of Physics, College of Education for Pure Sciences, University of Babylon, Hilla, Iraq. [8]Department of Materials Science and Engineering, Le Quy Don Technical University, Ha Noi 100000, Vietnam. [9]Department of Electrical and Computer Engineering, Sungkyunkwan University, 16419 Suwon, Korea. ✉email: bafekry.asad@gmail.com; mitragh@skku.edu

size and shape to produce custom geometries for nanostructures potentially useful for quantum computers, spintronics, electrothermal computing, and optoelectronics[17–20].

Meanwhile, the layered semiconductor chalcogenides belonging to the V-VI family has drawn significant attention due to its exceptional properties, such as earth-abundant constituents, low toxicity[21,22], optical, electronic and thermoelectric properties[23]. According to their semiconducting nature, these material allow overcoming the deficiencies of zero-bandgap in the graphene, showing gorgeous potential for building memory switching[24], microelectronics, and photovoltaic devices[25,26]. Among semiconductor chalcogenides, antimony-based materials, specifically, the antimony (Sb)- sulphide (S), selenide (Se), telluride (Te) like $Sb_2S_3$, $Sb_2Se_3$, and $Sb_2Te_3$ have drawn extensive attention, which can be considered as binary metal chalcogenide semiconducting materials with high stability. Moreover, the Earth's crust has an abundance of S, Se, Te and Sb elements of 260, 0.05, 0.005, and 0.2 ppm, respectively[27]. These monolayers possess distinctive crystal structures with semi-one-dimensional ribbons (chains) bound by vdWs, for instance, $(Sb_4Se_6)n$ ribbons in $Sb_2Se_3$[28,29]. This type of ribbon-structure contributes to strongly anisotropic charge transport. Besides, $Sb_2Te_3$ has both face-centred cubic and trigonal[30], and can be found in the liquid state and show high electron density states due to the delocalized electrons at Fermi level[31]. This is disaccorded from the conventional cubic materials with isotropic transport, such as GaAs, Si, Cu(In, Ga)$Se_2$, CdS, and CdSe, and perovskites ($CH_3NH_3PbI_3$)[32–34]. This makes the materials with the like-ribbons structure are preferable in solar cell applications. The $Sb_2S_3$ have drawn considerable attention, and extensively used for photovoltaic applications[35–38], photodetectors[39], sodium-ion batteries[40], and switching[41] because of its has sufficient elemental storage, tuning of band gap, high current ON/OFF ratio, great dipole moment, higher reversible theoretical capacity, possibility of solution, non-toxicity, mechanical and strong moisture stability at different temperatures[42–46]. $Sb_2S_3$ also shows remarkably an adequate physical criteria for photovoltaic light absorption materials with reasonable efficiencies in power conversion up to 7.5% [47–49]. However, Cai and Chen showed that the comparatively low power conversion of $Sb_2S_3$-based solar cells is mainly as a result of high resistivity of $Sb_2S_3$[50].

Similarly to $Sb_2S_3$, $Sb_2Se_3$ has recently received great attention to be utilized in applications of batteries[51,52], photoelectrical[53,54], thermoelectric devices[55] and photovoltaic light absorber[56], due to its prodigious properties such as an optimal bandgap (1-1.3 eV)[57,58], hole mobility up to 42 $cm^2V^{-1}s^{-1}$[59], desirable environmental characteristic[60,61], physiochemical stability[41], low-cost[62], and elevated thermoelectric power[24], as well as interesting optoelectronic features with absorption coefficient larger than 105 $cm^{-1}$ (at short wavelength)[27,63]. Also, a good efficiency in the power conversion up to 9.2% as very recently reported by Li et al.[64] On the other hand, $Sb_2Te_3$ is receiving growing research attention within the scientific community because of its gorgeous properties such as low crystallization temperature[65], and topological insulators[66]. Indeed, $Sb_2Te_3$ chips have already been reported for many applications such as the template materials[65], lithium-ion batteries[67], fast memory switching[68], and thermoelectric devices[69,70]. However, the states of the surface present in the $Sb_2Te_3$ isostructural compounds as the Dirac cone at around the Brillouin zone center (Γ-point) with a spin texture in charge of fascinating properties like comparative insensitivity to surface information[71,72]. On the other hand, Jiang et al. show that $Sb_2Te_3$ exhibited great characteristics of surface states relevant with Landau level transitions due to their extremely low carrier densities. Besides, the surface states are significantly changed by the asymmetry of the electron-hole from the bulk bands, resulting in the change of the Dirac point and the asymmetry of the band between the and the valence and conduction surface states[73]. Surprisingly, the $Sb_2X_3$ (X= S, Se, Te) were fabricated and experimentally prepared by vacuum thermal evaporation[74–76], electrodeposition[59], pulsed laser deposited[77], spray pyrolysis[78,79], epitaxy[80], and chemical deposition[81–83]. These experimental studies have demonstrated that $Sb_2X_3$(X= S, Se, Te) can be efficiently used as potential material for various applications.

Despite the hexagonal $Sb_2X_3$ (X = S, Se, Te) monolayers were under comprehensive researches over the past years based on the encouraging reports on their excellent properties, the physical properties of novel orthorhombic $Sb_2X_3$ (X = S, Se, Te) monolayers still undiscovered. Hence, we investigated in the present work the structural, electronic, optical, thermoelectric properties ofnovel $Sb_2X_3$ (X = S, Se, Te) monolayers crystallize in the orthorhombic structures by the density functional theory (DFT). Furthermore, for many related uses, the properties reported in this research may enable engineers and technicians to design and manufacture special types of modern nanoelectronics and optoelectronics devices.

## Method

The density-functional theory (DFT) calculations in this work are performed using the plane-wave basis projector augmented wave (PAW) method along with generalized gradient approximation (GGA) with Perdew-Burke-Ernzerhof(PBE)[84,85] functional as implemented in the Vienna *ab-initio* Simulation Package (VASP)[86,87]. Moreover, for the band structure calculations spin-orbit-coupling (SOC) was included on top of GGA and Heyd-Scuseria-Ernzerhof (HSE06)[88] screened-nonlocal-exchange functional of the generalized Kohn-Sham scheme, respectively for more accurate band gap calculations. The kinetic energy cut-off of 500 eV was set for plane-wave expansion and the energy was minimized structures are obtained until variation in the energies fall below $10^{-8}$ eV. Van der Waals (vdW) correction proposed by Grimme to describe the long-range vdW interactions[89]. Charge transfers analysis is accomplished using the Bader technique[90]. To get optimized structures, total Hellmann-Feynman forces were reduced to $10^{-7}$ eV/Å. 21 × 21×1 Γ centered *k*-point sampling was used or the primitive unit cells by using Monkhorst-Pack[91]. In this work, the phonon dispersion relations are acquired using machine-learning interatomic potentials on the basis of moment tensor potentials (MTPs)[92]. The training sets are prepared by conducting ab-initio molecular dynamics (AIMD) simulations over 4 × 2×1 supercells with 2 × 2×1 k-point grids and a time step of 1 fs. AIMD simulations are carried out at 50 and 600 K, each for 800 time steps and half of the full trajectories are selected to create the training sets. MTPs were then passively fitted using the methodology explained in the previous works[93,94]. The PHONOPY code[95] is employed to obtain phonon dispersion

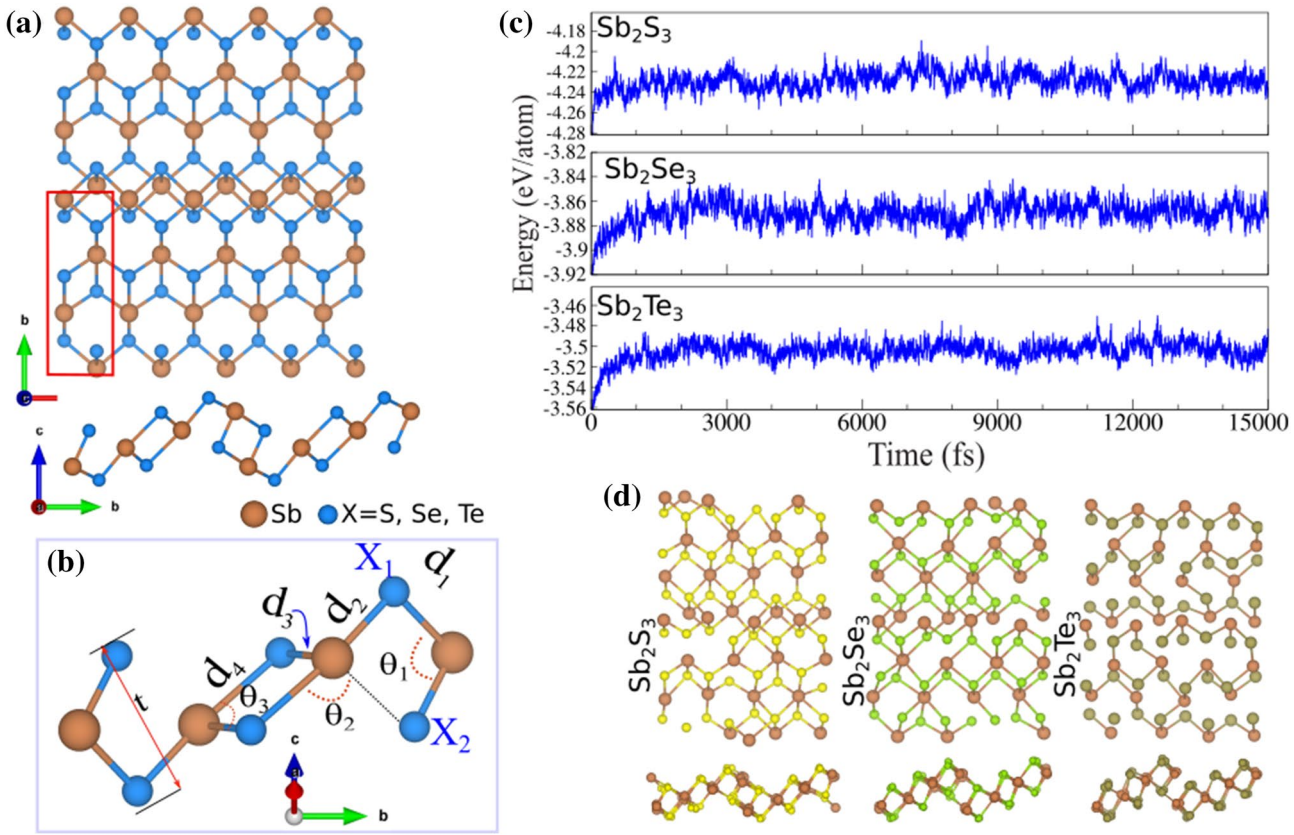


**Figure 1.** (**a**) Different views of atomic structure of $Sb_2X_3$ (X = S, Se, Te) monolayer, with the unit cell distinguished with a rectangle. (**b**) Schematic of structural parameters in a $Sb_2X_3$ lattice. (**c**) Ab initio molecular dynamics (AIMD) for these monolayers at room temperature. (**d**) The top and side views of the structures after 5 ps of simulation.

relations and harmonic force constants over 4 × 12×1 supercells using the trained MTPs for the interatomic force calculations[93,94]. The optical properties, such as imaginary and real parts of dielectric tensor (Im($\varepsilon$) and Re($\varepsilon$)), absorption coefficient ($\alpha$), reflectivity (R) Random phase approximation (RPA)[?] method on the basis of screened hybrid Heyd-Scuseria-Ernzerhof functional (HSE06)[88] was employed to study optical properties using the VASP[86,87]. The optical properties were evaluated using a dense k-point grid of 18 × 8×1 Γ-centered Monkhorst-Pack[91]. For more details about calculations of optical properties see supporting information. The electrical transport coefficients, such as electrical conductivity ($\sigma$), Seebeck coefficient ($S$), and electronic thermal conductivity ($\kappa_e$) are calculated using the Boltzmann transport equation as implemented in the Boltztrap2 code[96] under the constant relaxation time and rigid band approximations.

## Structural properties

The geometrical atomic structures of $Sb_2X_3$ (X = S, Se, Te) monolayers in the different views are depicted in Fig. 1a. The primitive unit cell of the $Sb_2X_3$ monolayers is indicated by red rectangular and is formed by 10 atoms with space group *Pmcn*. In the crystal structure of $Sb_2X_3$, each Sb atom is encompassed by six X (X = S, Se, Te) atoms and each X atom is encompassed by four Sb atoms. Notice that the vectors $\vec{a} \neq \vec{b}$ are the translational unit cell vectors. The calculated lattice parameters of $a$ ($b$) in the $Sb_2S_3$, $Sb_2Se_3$ and $Sb_2Te_3$ monolayers are equal to 3.86 (10.92), 3.92 (9.99) and 3.87 (9.65) Å, respectively, as listed in Table 1. Notice that the bond lengths $d_{1,2}$ and $d_{3,4}$ are determined to be 2.66/2.59 Å and 2.56/4.94 Å for $Sb_2S_3$ monolayer, 2.75/2.90 Å and 2.77/4.97 Å for $Sb_2Se_3$ monolayer, 2.95/3.13 Å and 2.99/3.02 Å for $Sb_2Te_3$ monolayer, respectively. The two angles of X-Sb-X in lattice of $Sb_2S_3$, $Sb_2Se_3$ and $Sb_2Te_3$ are 91/106/86°, 95/90/92° and 97/86/94°, respectively, which result in high anisotropic lattice. The thickness of $Sb_2S_3$, $Sb_2Se_3$ and $Sb_2Te_3$ monolayers are calculated to be 3.17, 3.66 and 3.79 Å, respectively.

The difference charge density ($\Delta\rho$) is defined as:

$$\Delta\rho = \rho_{tot} - \rho_X - \rho_{Sb} \tag{1}$$

where $\rho_{tot}$, $\rho_X$ and $\rho_{Sb}$ show charge densities of the $Sb_2X_3$ and isolated atoms, respectively. It is clear that Sb atoms are positively charged and surrounded by negatively charged S, Se or Te atoms. Each S, Se and Te atom labeled $X1(X2)$ (see Fig. 1b), gains about 0.75$e$ (0.82$e$), 0.59$e$ (0.64$e$) and 0.36$e$ (0.37$e$) from the adjacent Sb atoms in

| | $a$ $(b)$ (Å) | $d_{1/2}$ (Å) | $d_{3/4}$ (Å) | $t$ (Å) | $\theta_{1/2/3}$ (°) | $E_{coh}$ (eV/atom) | $\Delta Q$ (e) | $\Phi$ (eV) | $E_g$ (eV) |
|---|---|---|---|---|---|---|---|---|---|
| $Sb_2S_3$ | 3.86 (10.92) | 2.66/2.59 | 2.56/4.94 | 3.17 | 91/106/86 | − 7.94 | 0.75 (0.82) | 5.17 | 1.22 (2.15) |
| $Sb_2Se_3$ | 3.92 (9.99) | 2.75/2.90 | 2.77/4.97 | 3.66 | 95/90/92 | − 7.36 | 0.59 (0.64) | 4.94 | 0.96 (1.35) |
| $Sb_2Te_3$ | 3.87 (9.65) | 2.95/3.13 | 2.99/3.02 | 3.79 | 97/86/94 | − 6.81 | 0.36 (0.37) | 4.53 | 0.86 (1.37) |

**Table 1.** Structural and electronic parameters of $Sb_2X_3$ (X = S, Se, Te) monolayers as shown in Fig. 1b, including lattice constants **a**, $b$; the bond lengths between Sb-X atoms $d_{1,2,3,4}$; the bond angles between X-Sb-X atoms $\theta_{1,2,3}$; the thickness defined by the difference between the largest and smallest z coordinates of X atoms ($t$); the cohesive energy per atom, ($E_{coh}$); the charge transfer ($\Delta Q$) between atoms Sb and $X_1$ ($X_2$) atoms are shown inside (outside) parentheses as shown in Fig. 1b; the work function ($\Phi$). The band gap ($E_g$) of PBE and HSE06 are shown outside and inside parentheses, respectively.

$Sb_2S_3$, $Sb_2Se_3$ and $Sb_2Te_3$, respectively. Worthy to note that the charge redistribution stem from different electronegativities of 2.05 (Sb), 2.58 (S), 2.55 (Se) and 2.1 (Te).

Cohesive energy, which is defined as the energy required to separate condensed material into isolated free atoms, is one of the most important physical parameters in quantifying the energetic stability of materials. The cohesive energy per atom is calculated using the following equation:

$$E_{coh} = \frac{E_{tot} - 3E_X - 2E_{Sb}}{n_{tot}} \tag{2}$$

where $E_X$ and $E_{Sb}$ represent the energies of isolated single X (S, Se and Te) and Sb atoms, $n_{tot}$ is the total number of atoms in unit cell. $E_{tot}$ represents the total energy of the $Sb_2X_3$ monolayer. The cohesive energy of $Sb_2S_3$ and $Sb_2Se_3$ are found to be -7.94 and -7.36 eV/atom, respectively. While the cohesive energy of $Sb_2Te_3$ is -6.81 eV/atom. These finding indicates that the formation of $Sb_2S_3$ is more favorable than the others. The results of Ab initio molecular dynamics (AIMD) simulation for the studied monolayers at room temperature are shown in Fig. 1c. The snapshots of top and side views of the structures after 5 ps are illustrated in Fig. 1d. Analysis of the AIMD trajectories also shows that the structure could stay intact at 500 K with very stable energy and temperature profiles, proving the thermal stability of the $Sb_2X_3$ monolayer.

Apparently, phonon branches are free from any imaginary frequencies indicating the dynamical stability of the structures. The more negative values for cohesive energies suggest that the energetically more stable monolayer, and the structures represent more stability when the atoms get lighter. The dynamical stability of single-layers of $Sb_2X_3$ is verified by calculating their phonon band dispersions through the whole BZ which are presented in Fig. 2a–c.

The electrostatic potential for the $Sb_2X_3$ monolayers is shown in Fig. 2d. Notice that the electrostatic potential of studied monolayers are flat in the vacuum region. The work function was calculated using the following $\Phi = E_{vacuum} - E_F$, where $E_{vacuum}$ is the energy of the vacuum which is extracted from the electrostatic potential, and $E_F$ is the Fermi energy. The calculated work function of the studied monolayers are 5.17 ($Sb_2S_3$), 4.94 ($Sb_2Se_3$) and 4.53 eV ($Sb_2Te_3$). We found that the work function is decreases as the electronegativity of X (X = S, Se and Te) atom decreases.

## Electronic properties

The electronic band structure of $Sb_2X_3$ monolayers are shown in Fig. 3a. Our results show that, $Sb_2S_3$ is an indirect semiconductor with a band gap of 1.22 eV within PBE functional. Notice that the valance band minimum (VBM) is located at the Γ point, while the conduction band maximum (CBM) is located along the Γ-S points. Similar $Sb_2S_3$, $Sb_2Se_3$ and $Sb_2Te_3$ exhibit semiconducting characteristics with indirect band gap of 0.96 eV and 0.86 eV, respectively. Notice that, we can see that both the VBM and CBM of these monolayers are located along the Γ and Y points, respectively. The electronic band structure of $Sb_2X_3$ monolayers with considering spin orbital coupling (SOC) are shown in Fig. S1a–c in the supplementary information (SI). With considering of SOC effect, the band gaps of the $Sb_2S_3$, $Sb_2Se_3$ and $Sb_2Te_3$ monolayers decrease to 0.95, 0.75 and 0.45 eV, respectively. The charge densities of the VBM and CBM orbitals are shown in the inset (see inset in Fig. 3a). It is clear that energy bands around the Fermi-level are formed mainly by X atoms. Since these monolayers are semiconductor, the HSE06 functional was also used to study the electronic band structures, shown in Fig. 3. It is clear that the HSE06 results are consistent with PBE/GGA for the type of indirect semiconducting band gap in these systems. Based on the acquired band structure by HSE06 method, the indirect band gap of $Sb_2S_3$, $Sb_2Se_3$ and $Sb_2Te_3$ was estimated to be 2.15, 1.35 and 1.37 eV, respectively. The band gap value of $Sb_2Te_3$ is still larger than that reported in Ref.[97]. The nature of such difference is due to the underestimation of traditional DFT method. Therefore, our calculations methods are reliable. In order to explain the origin of the electronic states, the DOS and the PDOS are shown in Fig. 3b,c, respectively. It is clearly seen that the semiconducting character of $Sb_2S_3$ comes from S and Te atoms, while Sb atoms does now show any contribution. From DOS and PDOS, it is clearly seen that the VBM are composed of the $p_z$ and $p_{x,y}$ orbitals states of S atom, while the CBM comes from $p_z$ and $p_{x,y}$ orbitals of S and Sb atoms. We found that the VBM of $Sb_2Se_3$ and $Sb_2Te_3$ originates from Se/Te-$p_{x,y}$ orbitals, while the CBM consists of Se/Te-$p_z$ and Sb-$p_z$ orbital states.

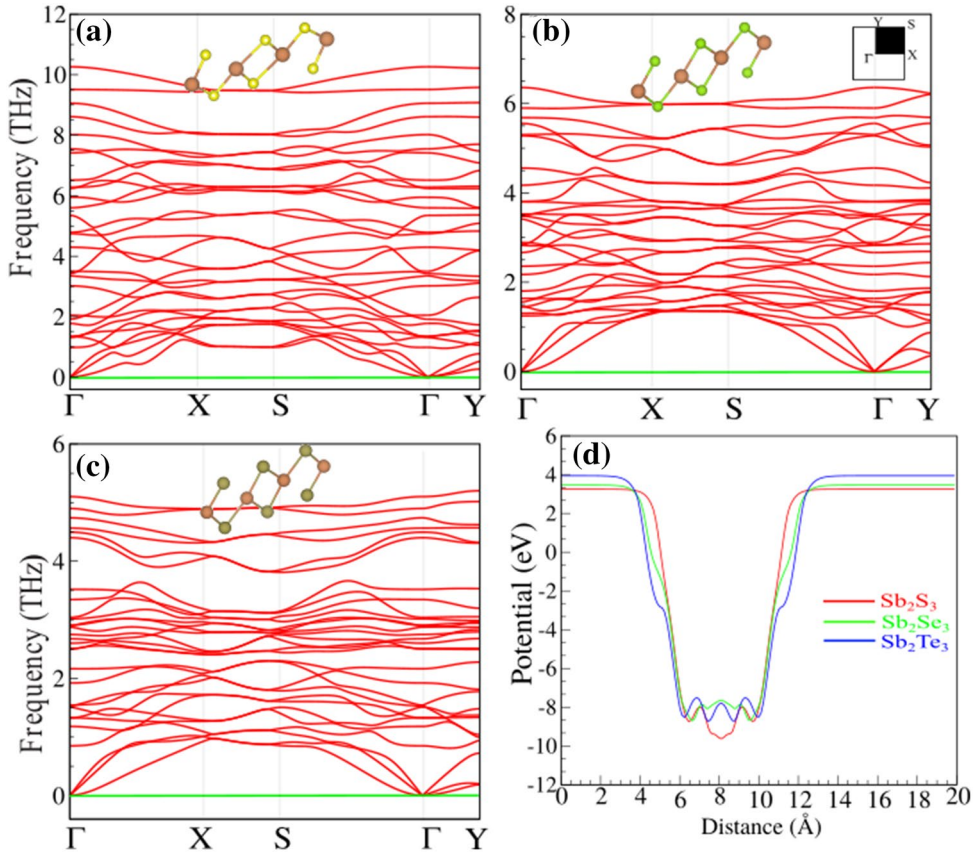


**Figure 2.** Phonon dispersions of (**a**) $Sb_2S_3$, (**b**) $Sb_2Se_3$ and (**c**) $Sb_2Te_3$ monolayers. Optimized atomic structure indicated as inset. (**d**) Electrostatic potential for the $Sb_2X_3$ monolayers.

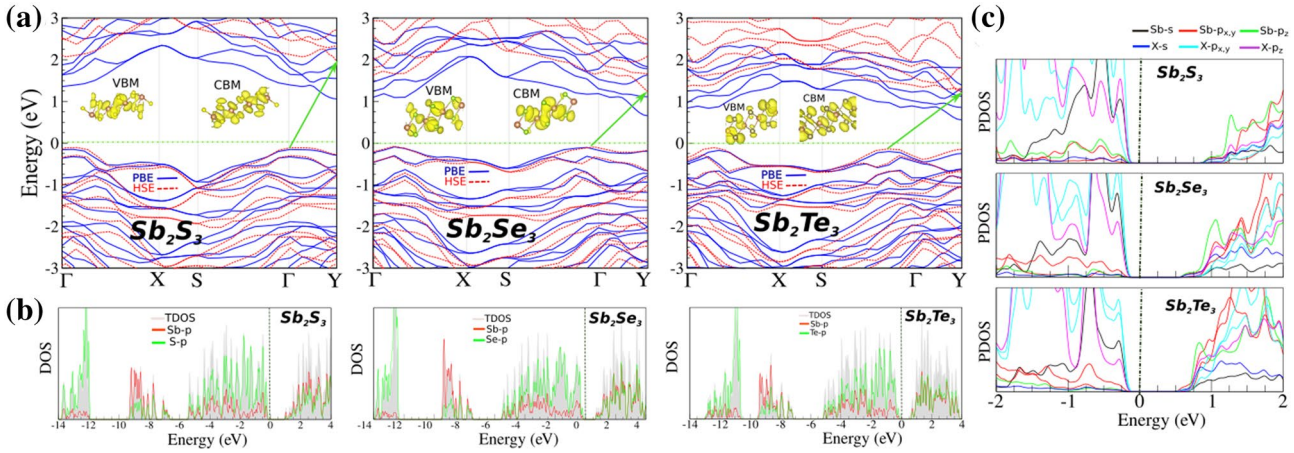


**Figure 3.** (**a**) Electronic band structure, (**b**) density of states (DOS) and (**c**) projected DOS (PDOS) of $Sb_2X_3$ monolayers. The zero of energy is set to Fermi-level.

## Optical properties

Now we discuss the optical responses of this novel 2D system using the RPA+ HSE06. The depolarization effect of 2D materials along out-of-plane direnction is strong[98], hence we only report the optical properties for in-plane polarizations (E ∥ x and E ∥ y). Due to the asymmetric lattice along the x- and y-directions the optical properties are aisotropic for light polarizations along these axes and hence the optical properties along both directions are reported. Fig. 4a illustrates the imaginary and real parts of the dielectric function of these 2D systems along the in-plane directions. It can be seen that the Im($\varepsilon$) along x- and y-axes starts with a gap confirming the semiconducting properties for optical spectra along these directions for these novel 2D systems. The first peak of

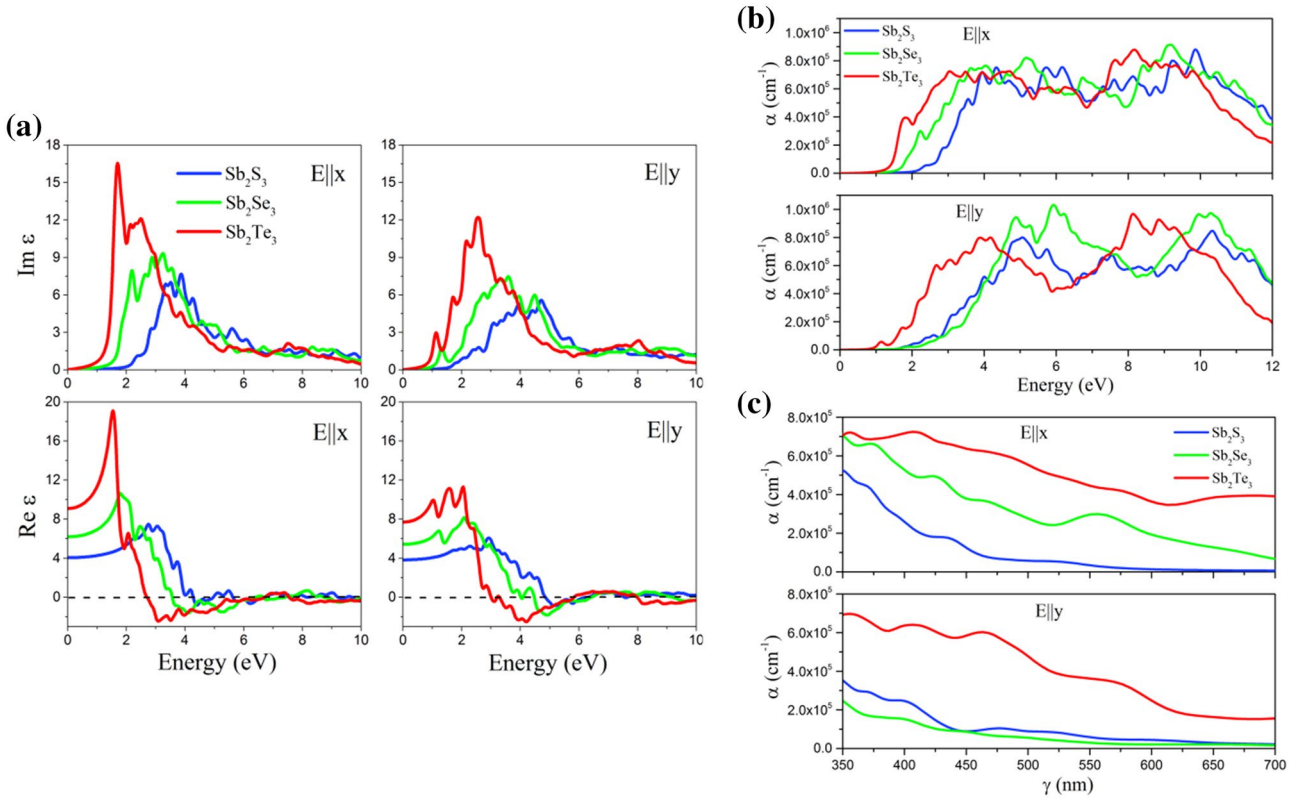


**Figure 4.** (**a**) Imaginary and real parts of the dielectric function as a function of photon energy of the $Sb_2S_3$, $Sb_2Se_3$ and $Sb_2Te_3$ monolayers for the in-plane polarizations (E ∥ x and E ∥ y), predicted using the RPA + HSE06 approach. Absorption coefficient as a function of (**b**) wavelength and (**c**) energy for the $Sb_2X_3$ monolayers for the in-plane polarizations (E ∥ x and E ∥ y) in the UV–vis range of light, predicted using the RPA + HSE06 approach.

Im($\varepsilon$) occurs at 2.39, 2.16 and 1.67 eV for the $Sb_2S_3$, $Sb_2Se_3$ and $Sb_2Te_3$ monolayers, respectively, along x-axis while it appears at 1.74, 1.36 and 1.10 eV along y-axis. These results indicate that the first peaks of Im($\varepsilon$) for all monolayer systems are in visible and *IR* range of light along talong x- and y-axes. These results also indicate that by increasing atomic number of X element in $Sb_2X_3$ monolayers, the first Im($\varepsilon$) peak slightly shifts to lower energies (red shift). The static dielectric constants (the values of Re($\varepsilon$) at zero energy) for $Sb_2Te_3$ monolayer along E ∥ x were calculated to be 4.0, 6.4 and 9.1, respectively, while the corresponding values for E ∥ y are 3.9, 5.5 and 7.8. The plasma frequencies which define by the roots of Re($\varepsilon$) with x = 0 line[99,100] were calculated for these 2D monolayers. The values of first plasma frequencies along x-axis are 4.27, 3.51 and 2.65 eV for $Sb_2S_3$, $Sb_2Se_3$ and $Sb_2Te_3$ monolayers, respectively, while the corresponding values for the same systems along E ∥ y are 4.8, 4.45 and 2.98 eV. The absorption coefficient $\alpha$ for all studied 2D systems along in-plane polarization are shown in Fig. 4b,c. The first absorption peaks for the $Sb_2S_3$, $Sb_2Se_3$ and $Sb_2Te_3$ monolayers along E ∥ x are in the visible range of light and occur at energy of 2.39, 2.18 and 1.77 eV, respectively. The corresponding values of the first absorption peaks along y-axis locate at energy of 1.98, 2.13 and 1.14 eV for the same monolayers. These results show the first absorption peaks of $Sb_2S_3$ and $Sb_2Se_3$ monolayers for E ∥ y are in visible range of light while it occur at *IR* range for $Sb_2Te_3$ monolayer. According to our optical results, these 2D systems have potential applications in optoelectronic devices in the visible and *IR* spectral range. Fig. 4b illustrates the absorption coefficient as a function of wavelength for the $Sb_2X_3$ monolayers for the in-plane polarizations in the UV-vis range (350-700 nm) of light. It is obvious that the absorption coefficients for these 2D materials are high ($\sim 10^5 cm^{-1}$) to be used in optical devices[101]. Interestingly, optically anisotropic character of these systems along x- and y-axes is highly desirable for the design of polarization-sensitive photodetectors[102].

## Thermoelectric properties

The Seebeck coefficients as a function of carrier concentration for $Sb_2X_3$ monolayers are presented in Fig. 5a,b. Large Seebeck coefficients are found for the *p*-type doping in these monolayers due to the flat valence band which increases the density of states near the Fermi level. Monolayer $Sb_2S_3$ achieves higher Seebeck coefficient values of 530 $\mu VK^{-1}$, 483 $\mu VK^{-1}$ at 300 K along the *x* and *y* directions, respectively. The variation in electrical conductivity ($\sigma/\tau$) and the electronic thermal conductivity ($\kappa^e/\tau$ ) with respect to carrier concentration are plotted in Fig. 5c–f. The $\sigma/\tau$ and $\kappa^e/\tau$ of *n*-type are larger than that of the *p*-type one at the same doping level because of the dispersive conduction bands which lower the effective mass. The $\sigma/\tau$ and $\kappa^e/\tau$ follow the Wiedemann–Franz law. The $\sigma/\tau$ exhibits anisotropic behavior where the $\sigma/\tau$ value along the x-direction is higher than that alone the y-direction because of the dispersive band nature along Γ-X than Γ-Y direction. The power-factor (PF) ($S^2\sigma/\tau$)

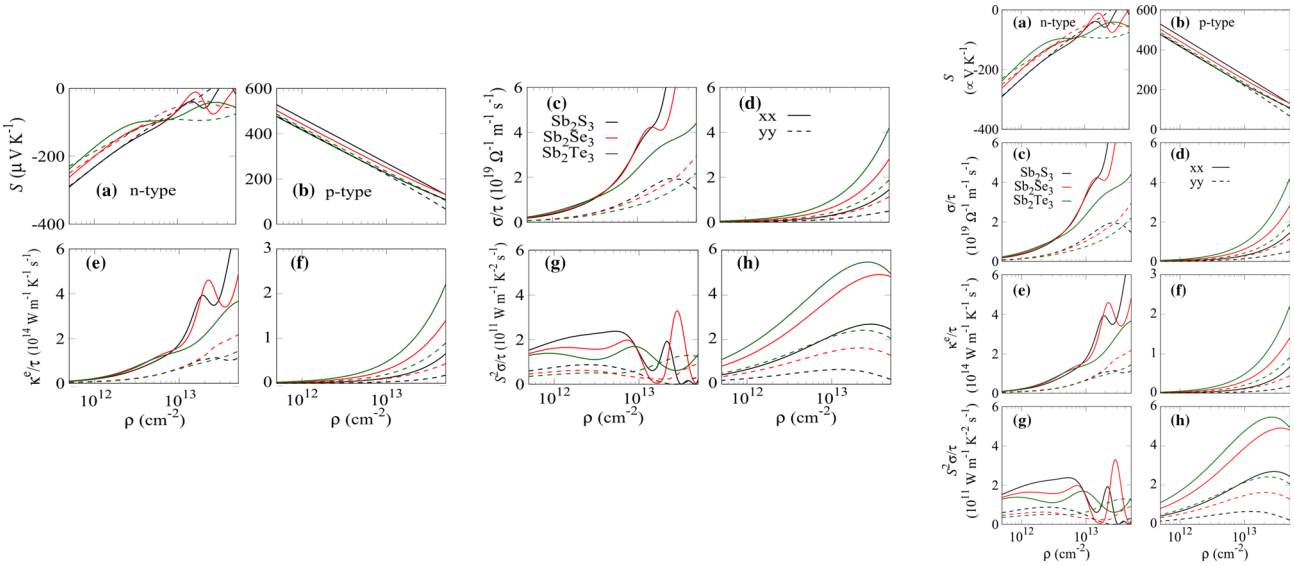


**Figure 5.** The electrical transport properties as function carrier concentration at 300 K of the $Sb_2X_3$ monolayers (**a**,**b**) Seebeck coefficient, (**c**,**d**) electrical conductivity, (**e**,**f**) electronic thermal conductivity, and (**g**,**h**) power factor. The solid and dashed lines represent the x-and y-direction, respectively.

is obtained using the calculated Seebeck coefficient and electrical conductivity as shown in Fig. 5g,h. For *p*-type monolayer $Sb_2Te_3$, the maximum *PF* values of 5.45 and 2.44 ($10^{11}\,Wm^{-1}K^{-2}s^{-1}$) are obtained at 300 K along the *x* and *y* directions. The value of *PF* is higher for the p-type doping because of large Secbeck coefficients. These values are significantly larger, demonstrating great potential as a promising candidate for thermoelectricity.

## Conclusion

In summary, we introduced $Sb_2X_3$ (X = S, Se, and Te) monolayers as novel, dynamically and thermally stable 2D indirect gap semiconductors. Using the HSE06 method the band gaps of $Sb_2S_3$, $Sb_2Se_3$ and $Sb_2Te_3$ monolayers are predicted to be 2.15, 1.35 and 1.37 eV, respectively, appealing for applications in nanoelectronics. Optical calculations indicate that the first absorption peaks of these novel nanosheets along in-plane polarization are located in IR and visible range of light, suggesting its prospect for applications in optoelectronics. Moreover, the in-plane optical anisotropy of these novel 2D materials is highly desirable for the design of polarization-sensitive photodetectors. We also show that $Sb_2X_3$ monoalyers can be used for thermoelectric application because of their larger power factors, the power factor for the hole-doped $Sb_2Te_3$ can reach 5.45 ($10^{11}\,Wm^{-1}K^{-2}s^{-1}$). Our results confirm the stability and highlights the outstanding prospect for the application of $Sb_2X_3$ nanosheets in novel electronic, optical and energy conversion systems.

Received: 18 February 2021; Accepted: 28 April 2021
Published online: 14 May 2021

## References

1. Qiu, Y. *et al.* Realizing high thermoelectric performance in GeTe through decreasing the phase transition temperature: Via entropy engineering. *J. Mater. Chem. A.* **7**, 26393–26401 (2019).
2. Shafique, A. & Shin, Y. H. Thermoelectric and phonon transport properties of two-dimensional IV–VI compounds. *Sci. Rep.* **7**, 1–10 (2017).
3. Hodges, J. M. *et al.* Chemical insights into PbSe- x%HgSe: High power factor and improved thermoelectric performance by alloying with discordant atoms. *J. Am. Chem. Soc.* **140**, 18115–18123 (2018).
4. Hien, N. D. *et al.* First principles study of single-layer $SnSe_2$ under biaxial strain and electric field: Modulation of electronic properties. *Phys. E Low-Dimens. Syst. Nanostruct.* **111**, 201–205 (2019).
5. Abdulraheem, Z. & Jappor, H. R. Tailoring the electronic and optical properties of $SnSe_2$/InS van der Waals heterostructures by the biaxial strains. *Phys. Lett. A.* **384**, 126909 (2020).
6. Velea, A. *et al.* Te-based chalcogenide materials for selector applications. *Sci. Rep.* **7**, 1–12 (2017).
7. Huang, Y. *et al.* Reliable exfoliation of large-area high-quality flakes of graphene and other two-dimensional materials. *ACS Nano.* **9**, 10612–10620 (2015).
8. Paton, K. R. *et al.* Scalable production of large quantities of defect-free few-layer graphene by shear exfoliation in liquids. *Nat. Mater.* **13**, 624–630 (2014).
9. Ambrosi, A., Sofer, Z., Luxa, J. & Pumera, M. Exfoliation of layered topological insulators $Bi_2Se_3$ and $Bi_2Te_3$ via electrochemistry. *ACS Nano.* **10**, 11442–11448 (2016).
10. Zheng, J. *et al.* High yield exfoliation of two-dimensional chalcogenides using sodium naphthalenide. *Nat. Commun.* **5**, 1–7 (2014).
11. Coleman, J. N. *et al.* Two dimensional nanosheets produced by liquid exfoliation of layered materials. *Science* **331**, 568–571 (2011).
12. Fathipour, S. *et al.* Exfoliated multilayer $MoTe_2$ field-effect transistors. *Appl. Phys. Lett.* **105**, 192101 (2014).

13. Li, H., Wu, J., Yin, Z. & Zhang, H. Preparation and applications of mechanically exfoliated single-layer and multilayer $MoS_2$ and $WSe_2$ nanosheets. *Acc. Chem. Res.* **47**, 1067–1075 (2014).
14. Sturala, J. *et al.* Exfoliation of calcium germanide by alkyl halides. *Chem. Mater.* **31**, 10126–10134 (2019).
15. Gusmao, R., Sofer, Z. & Pumera, M. Exfoliated layered manganese trichalcogenide phosphite ($MnPX_3$, X= S, Se) as electrocatalytic van der Waals materials for hydrogen evolution. *Adv. Funct. Mater.* **29**, 1805975 (2019).
16. Wood, J. D. *et al.* Effective passivation of exfoliated transistors against ambient degradation. *Nano Lett.* **14**, 6964–6970 (2014).
17. Friedensen, S., Mlack, J. T. & Drndic, M. Materials analysis and focused ion beam nanofabrication of topological insulator $Bi_2Se_3$. *Sci. Rep.* **7**, 1–7 (2017).
18. Bhattacharyya, B. *et al.* Observation of quantum oscillations in FIB fabricated nanowires of topological insulator ($Bi_2Se_3$). *J. Phys. Condens. Matter.* **29**, 115602 (2017).
19. Bhattacharyya, B., Awana, V. P. S., Senguttuvan, T. D., Ojha, V. N. & Husale, S. Proximity-induced supercurrent through topological insulator based nanowires for quantum computation studies. *Sci. Rep.* **8**, 17237 (2018).
20. Lopez-Sanchez, O., Lembke, D., Kayci, M., Radenovic, A. & Kis, A. Ultrasensitive photodetectors based on monolayer $MoS_2$. *Nat. Nanotechnol.* **8**, 497 (2013).
21. Obeid, M. M. *et al.* First-principles investigation of nonmetal doped single-layer BiOBr as a potential photocatalyst with a low recombination rate. *Phys. Chem. Chem. Phys.* **22**, 15354–15364 (2020).
22. Zhou, Y. *et al.* Thin-film $Sb_2Se_3$ photovoltaics with oriented one-dimensional ribbons and benign grain boundaries. *Nat. Photonics* **9**, 409–415 (2015).
23. Ovsyannikov, S. V. & Shchennikov, V. V. High-pressure routes in the thermoelectricity or how one can improve a performance of thermoelectrics. *Chem. Mater.* **22**, 635–647 (2010).
24. Platakis, N. S. & Gatos, H. C. Threshold and memory switching in crystalline chalcogenide materials. *Phys. Status Solidi* **13**, K1–K4 (1972).
25. Fourspring, P. M., DePoy, D. M., Rahmlow, T. D., Lazo-Wasem, J. E. & Gratrix, E. J. Optical coatings for thermophotovoltaic spectral control. *Appl. Opt.* **45**, 1356–1358 (2006).
26. He, M., Zheng, D., Wang, M., Lin, C. & Lin, Z. High efficiency perovskite solar cells: From complex nanostructure to planar heterojunction. *J. Mater. Chem. A.* **2**, 5994–6003 (2014).
27. Zhou, Y. *et al.* Solution-processed antimony selenide heterojunction solar cells. *Adv. Energy Mater.* **4**, 1301846 (2014).
28. Guo, L. *et al.* Tunable quasi-one-dimensional ribbon enhanced light absorption in $Sb_2Se_3$ thin-film solar cells grown by close-space sublimation. *Sol. RRL* **2**, 1800128 (2018).
29. Ma, J. *et al.* Controlled synthesis of one-dimensional $Sb_2Se_3$ nanostructures and their electrochemical properties. *J. Phys. Chem. C.* **113**, 13588–13592 (2009).
30. Zheng, Y. *et al.* Direct observation of metastable face-centered cubic $Sb_2Te_3$ crystal. *Nano Res.* **9**, 3453–3462 (2016).
31. Cobelli, M., Galante, M., Gabardi, S., Sanvito, S. & Bernasconi, M. First-principles study of electromigration in the metallic liquid state of GeTe and $Sb_2Te_3$ phase-change compounds. *J. Phys. Chem. C.* **124**, 9599–9603 (2020).
32. Guo, L. *et al.* Scalable and efficient $Sb_2S_3$ thin-film solar cells fabricated by close space sublimation. *APL Mater.* **7**, 041105 (2019).
33. Hasan, M. R. *et al.* An antimony selenide molecular ink for flexible broadband photodetectors. *Adv. Electron. Mater.* **2**, 1600182 (2016).
34. Huang, M., Xu, P., Han, D., Tang, J. & Chen, S. Complicated and unconventional defect properties of the quasi-one-dimensional photovoltaic semiconductor $Sb_2Se_3$. *ACS Appl. Mater. Interfaces* **11**, 15564–15572 (2019).
35. Kondrotas, R., Chen, C. & Tang, J. $Sb_2S_3$ solar cells. *Joule* **2**, 857–878 (2018).
36. Itzhaik, Y., Niitsoo, O., Page, M. & Hodes, G. $Sb_2S_3$-sensitized nanoporous $TiO_2$ solar cells. *J. Phys. Chem. C* **113**, 4254–4256 (2009).
37. Savadogo, O. & Mandal, K. C. Studies on new chemically deposited photoconducting antimony trisulphide thin films. *Sol. Energy Mater. Sol. Cells* **26**, 117–136 (1992).
38. Cai, Z., Dai, C. M. & Chen, S. Intrinsic defect limit to the electrical conductivity and a two-step p-type doping strategy for overcoming the efficiency bottleneck of $Sb_2S_3$-based solar cells. *Sol. RRL* **4**, 1900503 (2020).
39. Zhong, M. *et al.* High-performance photodetectors based on $Sb_2S_3$ nanowires: Wavelength dependence and wide temperature range utilization. *Nanoscale* **9**, 12364–12371 (2017).
40. Hameed, A. S., Reddy, M. V., Chen, J. L. T., Chowdari, B. V. R. & Vittal, J. J. RGO/stibnite nanocomposite as a dual anode for lithium and sodium ion batteries. *ACS Sustain. Chem. Eng.* **4**, 2479–2486 (2016).
41. Koc, H., Mamedov, A. M., Deligoz, E. & Ozisik, H. First principles prediction of the elastic, electronic, and optical properties of $Sb_2S_3$ and $Sb_2Se_3$ compounds. *Solid State Sci.* **14**, 1211–1220 (2012).
42. Xiong, X. *et al.* Enhancing sodium ion battery performance by strongly binding nanostructured $Sb_2S_3$ on sulfur-doped graphene sheets. *ACS Nano.* **10**, 10953–10959 (2016).
43. Bommier, C. & Ji, X. Recent development on anodes for Na-ion batteries. *Isr. J. Chem.* **55**, 486–507 (2015).
44. Yu, D. Y. W. *et al.* High-capacity antimony sulphide nanoparticle-decorated graphene composite as anode for sodium-ion batteries. *Nat. Commun.* **4**, 1–7 (2013).
45. Efthimiopoulos, I., Buchan, C. & Wang, Y. Structural properties of $Sb_2S_3$ under pressure: Evidence of an electronic topological transition. *Sci. Rep.* **6**, 1–9 (2016).
46. Cerdan-Pasaran, A., Lopez-Luke, T., Mathew, X. & Mathews, N. R. Effect of cobalt doping on the device properties of $Sb_2S_3$ -sensitized TiO2 solar cells. *Sol. Energy.* **183**, 697–703 (2019).
47. Wang, X., Tang, R., Wu, C., Zhu, C. & Chen, T. Development of antimony sulfide-selenide $Sb_2(S, Se)_3$-based solar cells. *J. Energy Chem.* **27**, 713–721 (2018).
48. Choi, Y. C., Lee, D. U., Noh, J. H., Kim, E. K. & Il Seok, S. Highly improved $Sb_2S_3$ sensitized-inorganic–organic heterojunction solar cells and quantification of traps by deep-level transient spectroscopy. *Adv. Funct. Mater.* **24**, 3587–3592 (2014).
49. Liu, Y. *et al.* Boosting potassium-ion batteries by few-layered composite anodes prepared via solution-triggered one-step shear exfoliation. *Nat. Commun.* **9**, 1–10 (2018).
50. Cai, Z. & Chen, S. Extrinsic dopants in quasi-one-dimensional photovoltaic semiconductor $Sb_2S_3$: A first-principles study. *J. Appl. Phys.* **127**, 183101 (2020).
51. Ou, X. *et al.* A new rGO-overcoated $Sb_2Se_3$ nanorods anode for Na+ battery: In situ X-ray diffraction study on a live sodiation/desodiation process. *Adv. Funct. Mater.* **27**, 1606242 (2017).
52. Tian, Y. *et al.* Low-bandgap sedeficient antimony selenide as a multifunctional polysulfide barrier toward high-performance lithium-sulfur batteries. *Adv. Mater.* **32**, 1904876 (2020).
53. Liang, G. X. *et al.* Facile preparation and enhanced photoelectrical performance of $Sb_2Se_3$ nano-rods by magnetron sputtering deposition. *Sol. Energy Mater. Sol. Cells* **160**, 257–262 (2017).
54. Wu, W.-Y., Xu, Y., Ong, X., Bhatnagar, S. & Chan, Y. Thermochromism from ultrathin colloidal $Sb_2Se_3$ nanowires undergoing reversible growth and dissolution in an amine-thiol mixture. *Adv. Mater.* **31**, 1806164 (2019).
55. Rahnamaye Aliabad, H. A. & Asadi Rad, F. Structural, electronic and thermoelectric properties of bulk and monolayer of $Sb_2Se_3$ under high pressure: By GGA and mBJ approaches. *Phys. B Condens. Matter* **545**, 275–284 (2018).
56. Wang, L. *et al.* Stable 6%-efficient $Sb_2Se_3$ solar cells with a ZnO buffer layer. *Nat. Energy* **2**, 1–9 (2017).

57. Filip, M. R., Patrick, C. E. & Giustino, F. GW quasiparticle band structures of stibnite, antimonselite, bismuthinite, and guanajuatite. *Phys. Rev. B Condens. Matter Mater. Phys.* **87**, 205125 (2013).
58. Zdanowicz, T., Rodziewicz, T. & Zabkowska-Waclawek, M. Theoretical analysis of the optimum energy band gap of semiconductors for fabrication of solar cells for applications in higher latitudes locations. *Sol. Energy Mater. Sol. Cells* **87**, 757–769 (2005).
59. Lai, Y. *et al.* Preparation and characterization of $Sb_2$ $Se_3$ thin films by electrodeposition and annealing treatment. *Appl. Surf. Sci.* **261**, 510–514 (2012).
60. Mavlonov, A. *et al.* A review of $Sb_2$ $Se_3$ photovoltaic absorber materials and thin-film solar cells. *Sol. Energy* **201**, 227–246 (2020).
61. Liang, G. X. *et al.* Thermally induced structural evolution and performance of $Sb_2$ $Se_3$ films and nanorods prepared by an easy sputtering method. *Sol. Energy Mater. Sol. Cells* **174**, 263–270 (2018).
62. Fleck, N. *et al.* Identifying Raman modes of $Sb_2$ $Se_3$ and their symmetries using angle-resolved polarised Raman spectra. *J. Mater. Chem. A* **8**, 8337–8344 (2020).
63. Wen, X. *et al.* Magnetron sputtered ZnO buffer layer for $Sb_2$ $Se_3$ thin film solar cells. *Sol. Energy Mater. Sol. Cells* **172**, 74–81 (2017).
64. Li, Z. *et al.* 9.2%-efficient core-shell structured antimony selenide nanorod array solar cells. *Nat. Commun.* **10**, 1–9 (2019).
65. Feng, J. *et al.* Stickier-surface $Sb_2$ $Te_3$ templates enable fast memory switching of phase change material $GeSb_2Te_4$ with growth-dominated crystallization. *ACS Appl. Mater. Interfaces* **12**, 33397–33407 (2020).
66. Zhang, H. *et al.* Topological insulators in $Bi_2Se_3$, $Bi_2Te_3$ and $Sb_2$ $Te_3$ with a single Dirac cone on the surface. *Nat. Phys.* **5**, 438–442 (2009).
67. Wei, Y. *et al.* Level the conversion/alloying voltage gap by grafting the endogenetic $Sb_2$ $Te_3$ building block into layered GeTe to build $Ge_2Sb_2Te_5$ for Li-ion batteries. *ACS Appl. Mater. Interfaces* **11**, 41374–41382 (2019).
68. Wuttig, M. & Yamada, N. Phase-change materials for rewriteable data storage. *Nat. Mater.* **6**, 824–832 (2007).
69. Snyder, G. J. & Toberer, E. S. Complex thermoelectric materials. *Nat. Mater.* **7**, 105–114 (2008).
70. Chen, Y. *et al.* New $Sb_2$ $Te_3$- xSex monolayers with high electron mobilities and wide absorption range. *ACS Appl. Mater. Interfaces* **11**, 37216–37228 (2019).
71. Hasan, M. Z. & Kane, C. L. Colloquium: Topological insulators. *Rev. Mod. Phys.* **82**, 3045–3067 (2010).
72. Campi, D., Bernasconi, M. & Benedek, G. Ab-initio calculation of surface phonons at the $Sb_2$ $Te_3$(111) surface. *Surf. Sci.* **678**, 46–51 (2018).
73. Jiang, Y. *et al.* Electron-hole asymmetry of surface states in topological insulator $Sb_2$ $Te_3$ thin films revealed by magneto-infrared spectroscopy. *Nano Lett.* **20**, 4588–4593 (2020).
74. Liu, X. *et al.* Thermal evaporation and characterization of $Sb_2$ $Se_3$ thin film for substrate $Sb_2$ $Se_3$/CdS solar cells. *ACS Appl. Mater. Interfaces* **6**, 10687–10695 (2014).
75. Debnath, R. K. & Fitzgerald, A. G. Electron beam induced surface modification of amorphous $Sb_2$ $S_3$ chalcogenide films. *Appl. Surf. Sci.* **243**, 148–150 (2005).
76. Shen, K. *et al.* Mechanisms and modification of nonlinear shunt leakage in $Sb_2$ $Se_3$ thin film solar cells. *Sol. Energy Mater. Sol. Cells* **186**, 58–65 (2018).
77. Xue, M. Z. & Fu, Z. W. Pulsed laser deposited $Sb_2$ $Se_3$ anode for lithium-ion batteries. *J. Alloys Compd.* **458**, 351–356 (2008).
78. Rajpure, K. Y., Lokhande, C. D. & Bhosale, C. H. Effect of the substrate temperature on the properties of spray deposited Sb-Se thin films from non-aqueous medium. *Thin Solid Films.* **311**, 114–118 (1997).
79. Bhosale, C. H., Uplane, M. D., Patil, P. S. & Lockhande, C. D. Preparation and properties of sprayed antimony trisulphide films. *Thin Solid Films* **248**, 137–139 (1994).
80. Lei, T. *et al.* Electronic structure of antimonene grown on $Sb_2$ $Te_3$ (111) and $Bi_2Te_2$ substrates. *J. Appl. Phys.* **119**, 015302 (2016).
81. Maghraoui-Meherzi, H., BenNasr, T. & Dachraoui, M. Synthesis, structure and optical properties of $Sb_2Se_3$. *Mater. Sci. Semicond. Process.* **16**, 179–184 (2013).
82. Li, S. *et al.* Effect of selenization temperature on the properties of $Sb_2$ $Se_3$ thin films and solar cells by two-step method. *J. Mater. Sci. Mater. Electron.* **30**, 19871–19879 (2019).
83. Sankapal, B. R., Mane, R. S. & Lokhande, C. D. Preparation and characterization of $Sb_2$ $S_3$ thin films using a successive ionic layer adsorption and reaction (SILAR) method. *J. Mater. Sci. Lett.* **18**, 1453–1455 (1999).
84. Perdew, J. P., Burke, K. & Ernzerhof, M. Generalized gradient approximation made simple. *Phys. Rev. Lett.* **77**, 3865 (1996).
85. Perdew, J. P., Burke, K. & Ernzerhof, M. Generalized gradient approximation made simple. *Phys. Rev. Lett.* **78**, 1396 (1997).
86. Kresse, G. & Hafner, J. Ab initio molecular dynamics for liquid metals. *Phys. Rev. B* **47**, 558 (1993).
87. Kresse, G. & Hafner, J. Efficient iterative schemes for ab initio total-energy calculations using a plane-wave basis set. *Phys. Rev. B* **49**, 14251 (1994).
88. Heyd, J., Scuseria, G. E. & Ernzerhof, M. Screened hybrid density functionals applied to solids. *J. Chem. Phys.* **118**, 8207 (2003).
89. Grimme, S. J. Semiempirical GGA-type density functional constructed with a long-range dispersion correction. *Comput. Chem.* **27**, 1787 (2006).
90. Henkelman, G., Arnaldsson, A. & Jonsson, H. A fast and robust algorithm for Bader decomposition of charge density. *Comput. Mater. Sci.* **36**, 354 (2006).
91. Monkhorst, H. J. & Pack, J. D. Special points for Brillouin-zone integrations. *Phys. Rev. B* **13**, 12 (1976).
92. Shapeev, A. V. Moment tensor potentials: A class of systematically improvable interatomic potentials. *Multiscale Model. Simul.* **14**, 1153–1173 (2016).
93. Mortazavi, B. *et al.* Exploring photonic properties of two-dimensional materials using machine learning interatomic potentials. *Appl. Mater. Today* **20**, 100685 (2020).
94. Mortazavi, B. *et al.* Accelerating first-principles estimation of thermal conductivity by machine-learning interatomic potentials: A MTP/Sheng BTE solution. *Comput. Phys. Commun.* **258**, 107583 (2021).
95. Togo, A. & Tanaka, I. First principles phonon calculations in materials science. *Scr. Mater.* **108**, 1–5 (2015).
96. Madsen, G. K. H., Carrete, J. & Verstraete, M. J. BoltzTraP2, a program for interpolating band structures and calculating semi-classical transport coefficients. *Comput. Phys. Commun.* **231**, 140–145 (2018).
97. Bin, Xu. *et al.* Thermoelectric properties of monolayer $Sb_2$ $Te_3$. *J. Appl. Phys.* **124**, 165104 (2018).
98. Shahrokhi, M. Quasi-particle energies and optical excitations of ZnS monolayer honeycomb structure. *Appl. Surf. Sci.* **390**, 377–384 (2016).
99. Shahrokhi, M., Naderi, S. & Fathalian, A. Ab initio calculations of optical properties of $B_2C$ graphene sheet. *Solid State Commun.* **152**, 1012–1017 (2012).
100. Shahrokhi, M. & Leonard, C. Tuning the band gap and optical spectra of silicon-doped graphene: Many-body effects and excitonic states. *J. Alloys Compd.* **693**, 1185e1196 (2017).
101. Shahrokhi, M., Raybaud, P. & Le Bahers, T. On the understanding of the optoelectronic properties of S-doped $MoO_3$ and O-doped $MoS_2$ bulk systems: a DFT perspective. *J. Mater. Chem. C* **8**, 9064–9074 (2020).
102. Shahrokhi, M. Can fluorine and chlorine functionalization stabilize the graphene like borophene?. *Comput. Mater. Sci.* **156**, 56–66 (2019).

## Acknowledgements
This work was supported by the National Research Foundation of Korea (NRF) grant funded by the Korea government (MSIT) (NRF-2015M2B2A4033123).

## Author contributions
A.B.: Conceptualization, Methodology, Software, Writing - original draft, Formal analysis, Visualization, Investigation, Supervision, Project administration. B.M.: Methodology, Software, Writing - original draft. M.F.: Methodology, Software, Investigation, Writing - original draft. M.S.: Methodology, Software, Writing. A.S.: Methodology, Software, Writing. H.R.J.: Writing - review editing. C.N.: Writing - original draft, Writing - review editing. M.G.: Writing - review editing, Supervision, Project administration. S.F.: Methodology, Software, Writing.

## Competing interests
The authors declare no competing interests.

## Additional information
**Supplementary Information** The online version contains supplementary material available at https://doi.org/10.1038/s41598-021-89944-4.

**Correspondence** and requests for materials should be addressed to A.B. or M.G.

**Reprints and permissions information** is available at www.nature.com/reprints.

**Publisher's note** Springer Nature remains neutral with regard to jurisdictional claims in published maps and institutional affiliations.